

This is a repository copy of *Efficient Silicon Metasurfaces for Visible Light*.

White Rose Research Online URL for this paper:

<https://eprints.whiterose.ac.uk/118859/>

Version: Accepted Version

---

**Article:**

Zhou, Zhenpeng, Li, Juntao, Su, Rongbin et al. (9 more authors) (2017) Efficient Silicon Metasurfaces for Visible Light. ACS Photonics. pp. 544-551. ISSN 2330-4022

<https://doi.org/10.1021/acsp Photonics.6b00740>

---

**Reuse**

Items deposited in White Rose Research Online are protected by copyright, with all rights reserved unless indicated otherwise. They may be downloaded and/or printed for private study, or other acts as permitted by national copyright laws. The publisher or other rights holders may allow further reproduction and re-use of the full text version. This is indicated by the licence information on the White Rose Research Online record for the item.

**Takedown**

If you consider content in White Rose Research Online to be in breach of UK law, please notify us by emailing [eprints@whiterose.ac.uk](mailto:eprints@whiterose.ac.uk) including the URL of the record and the reason for the withdrawal request.

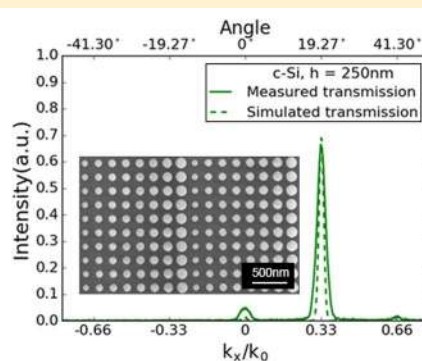
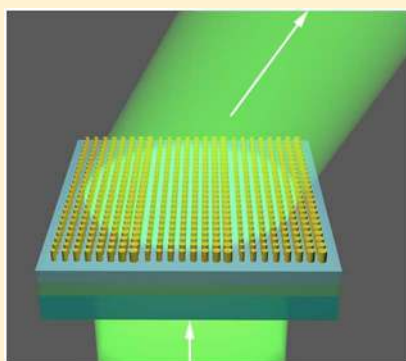
# Efficient Silicon Metasurfaces for Visible Light

Zhenpeng Zhou,<sup>†,‡,||</sup> Juntao Li,<sup>†,‡,||</sup> Rongbin Su,<sup>†,‡</sup> Beimeng Yao,<sup>†,‡</sup> Hanlin Fang,<sup>†,‡</sup> Kezheng Li,<sup>†,‡</sup>  
 Lidan Zhou,<sup>†</sup> Jin Liu,<sup>†,‡</sup> Daan Stellinga,<sup>§</sup> Christopher P. Reardon,<sup>§</sup> Thomas F. Krauss,<sup>†,§</sup>  
 and Xuehua Wang<sup>\*,†,‡</sup>

<sup>†</sup>State Key Laboratory of Optoelectronic Materials and Technologies and <sup>‡</sup>School of Physics, Sun Yat-Sen University, Guangzhou, 510275, China

<sup>§</sup>Department of Physics, University of York, York, YO10 5DD, U.K.

**S** Supporting Information



**ABSTRACT:** Dielectric metasurfaces require high refractive index contrast materials for optimum performance. This requirement imposes a severe restraint; either devices have been demonstrated at wavelengths of 700 nm and above using high-index semiconductors such as silicon, or they use lower index dielectric materials such as TiO<sub>2</sub> or Si<sub>3</sub>N<sub>4</sub> and operate in the visible wavelength regime. Here, we show that the high refractive index of silicon can be exploited at wavelengths as short as 532 nm by demonstrating a crystalline silicon metasurface with a transmission efficiency of 71% at this wavelength and a diffraction efficiency of 95% into the desired diffraction order. The metasurfaces consist of a graded array of silicon posts arranged in a square lattice on a quartz substrate. We show full  $2\pi$  phase control, and we experimentally demonstrate polarization-independent beam deflection at 532 nm wavelength. Our results open a new way for realizing efficient metasurfaces based on silicon for the technologically all-important display applications.

**KEYWORDS:** dielectric metasurfaces, crystalline silicon, wavefront control, diffractive optics

Metasurfaces are ultrathin optical elements that can manipulate optical wavefronts by modifying the phase, amplitude, or polarization of light waves on a subwavelength scale.<sup>1–6</sup> Metasurfaces offer new degrees of freedom for controlling light beams on a smaller scale and with higher accuracy than is possible with conventional bulky optical components. Initial demonstrations of metasurfaces involved plasmonic resonances, which, however, are rather lossy and exhibit low efficiency.<sup>7,8</sup> More recently, all-dielectric metasurfaces have come to the fore because of their high transmission.<sup>9–11</sup> Compared to plasmonic metasurfaces, they offer lower loss, yet they still exhibit Mie resonances for both polarizations at optical frequencies, which has been used to realize perfect reflectors,<sup>12</sup> magnetic mirrors,<sup>13</sup> and Huygens surfaces.<sup>14,15</sup>

Because of its high refractive index and compatibility with CMOS processes, silicon is widely used in all-dielectric metasurface devices, such as flat lenses,<sup>16–18</sup> achromatic lenses,<sup>19</sup> vortex generators,<sup>20,21</sup> holograms,<sup>22–25</sup> nonlinear

devices,<sup>26</sup> and metasurfaces controlled phase and polarization independently.<sup>27,28</sup> However, most of the silicon metasurface work is performed in the near-infrared wavelength regime and not in the visible. This is because most researchers use amorphous silicon (a-silicon) or polycrystalline silicon (poly-silicon) due to the ease of deposition onto transparent substrates such as glass. The problem with deposited silicon is its high absorption loss in the visible regime. Thin-film crystalline silicon (c-silicon) offers a solution to this problem because of its much lower absorption at  $\lambda > 500$  nm.<sup>29,30</sup> For example, the single-pass absorption of a 200 nm thin film of c-silicon and a-silicon is around 15% and 51% at a wavelength of 500 nm, respectively. The corresponding refractive index and extinction coefficient of c-silicon and a-silicon are  $n_{c-si} = 4.295$ ,  $k_{c-si} = 0.0719$ <sup>29</sup> and  $n_{a-si} = 4.497$ ,  $k_{a-si} = 0.45526$ .<sup>11</sup> While most researchers are aware that the absorption of c-silicon is lower

**Received:** September 28, 2016

**Published:** January 31, 2017

54 than that of a-silicon, it is not at all obvious that this difference  
 55 is sufficient to enable the successful demonstration of high-  
 56 efficiency metasurfaces in the visible regime. Metasurfaces must  
 57 create large phase delay in order to operate efficiently, and the  
 58 large phase delays are typically achieved with large aspect ratio  
 59 nanostructures. In the case of high refractive index absorbing  
 60 materials such as silicon, the question arises whether a sufficient  
 61 phase delay can be achieved in a given thickness of material  
 62 without excessive absorption. Since the phase delay and  
 63 absorption are a function of the entire nanostructure and not  
 64 the thin film alone, this question can be answered only by  
 65 considering the structure as a whole. Alternatively, titanium  
 66 dioxide ( $\text{TiO}_2$ ),<sup>31–33</sup> silicon nitride ( $\text{Si}_3\text{N}_4$ ),<sup>34</sup> and silica  
 67 ( $\text{SiO}_2$ )<sup>35</sup> have been used for all-dielectric metasurfaces based  
 68 on their high transparency throughout the visible spectrum. For  
 69 example, a 600 nm thin  $\text{TiO}_2$  film has recently been patterned  
 70 into nanofins and posts in order to form a high numerical  
 71 aperture (NA) metalens for operation at visible wave-  
 72 lengths.<sup>32,33</sup> Due to the lower refractive index contrast  
 73 compared to silicon, however, these  $\text{TiO}_2$  nanofins and posts  
 74 require very high aspect ratios of 10–15<sup>32</sup> and 6,<sup>33</sup> respectively,  
 75 which makes the fabrication very challenging.

76 Here, we propose the use of thin-film c-silicon as a  
 77 metasurface material for visible light operation and demonstrate  
 78 high efficiency polarization-independent operation in trans-  
 79 mission at 532 nm wavelength. This demonstration is enabled  
 80 by our layer-transfer technique, whereby we transfer 220 and  
 81 250 nm c-silicon device layers from a silicon on insulator (SOI)  
 82 wafer to a transparent quartz substrate. The maximum aspect  
 83 ratio of our metasurfaces is 3.4 in the experiment, which makes  
 84 it easier to fabricate than comparable devices based on  $\text{Si}_3\text{N}_4$  or  
 85  $\text{TiO}_2$ . We believe that this method will open a new way to  
 86 extend the functionalities of metasurfaces efficiently into the  
 87 visible light regime.

88 To illustrate the capability of our c-silicon metasurface in  
 89 transmission and its full  $2\pi$  phase control, we consider light  
 90 propagating through an array of circular c-silicon posts on a  
 91 subwavelength square lattice (Figure 1).<sup>16,27</sup> Each post acts as  
 92 Fabry–Pérot resonator, and different diameter posts support  
 93 modes of different effective index. Due to the circular symmetry  
 94 of the circular posts, our metasurfaces are polarization-  
 95 independent.

96 We performed the numerical calculation using the rigorous  
 97 coupled-wave analysis (RCWA) method<sup>36</sup> and analyzed the  
 98 transmission coefficient and phase of the periodic c-silicon  
 99 posts by varying the unit cell size  $a$  from 160 to 250 nm and the  
 100 diameter from  $0.2a$  to  $0.8a$  at the wavelength 532 nm (Figure  
 101 2a,b). In the calculation, the post height  $h$  is fixed to be 220 nm  
 102 (refractive index from ref 29), the thickness of the silica film  
 103 (refractive index  $n_{\text{Silica}} = 1.45$ ) and the adhesive NOA61  
 104 (Norland Products, Inc.) ( $n_{\text{NOA}} = 1.56$ ) underneath are  $1\ \mu\text{m}$ ,  
 105 and the refractive index of the quartz substrate is 1.45. As  
 106 shown in Figure 2, arrays of posts with 190 nm unit cell size can  
 107 achieve large transmission amplitudes while spanning the full  
 108 range of phases from 0 to  $2\pi$  by varying the diameter of the  
 109 posts from 38 to 152 nm. In Table 1, which is based on Figure  
 110 2c, we choose eight different diameter posts with  $\pi/4$   
 111 increments to cover the full 0 to  $2\pi$  phase range.

112 To validate the phase control effect of our c-silicon  
 113 metasurfaces, we designed a prism-like refractive index gradient  
 114 as a beam deflector using the eight phase elements shown in  
 115 Table 1. The diffraction angle  $\theta_t$  of such a gradient surface can  
 116 be calculated via the generalized Snell's law,<sup>8</sup>

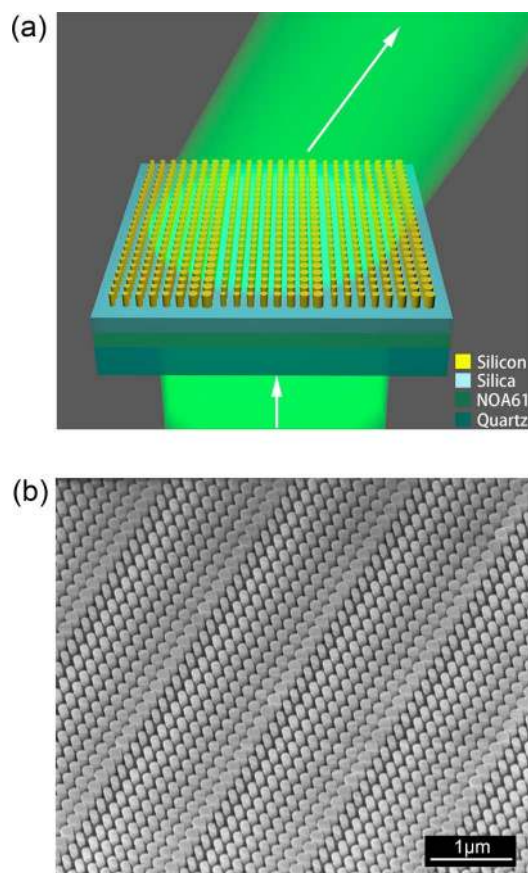


Figure 1. (a) Schematic of a gradient metasurface that acts as a beam deflector and (b) an SEM micrograph of our metasurface structure.

$$n_t \sin \theta_t - n_i \sin \theta_i = \frac{\lambda}{2\pi} \frac{d\Phi}{dx} \quad (1)$$

where  $n_t$  and  $n_i$  are the refractive index of the surrounding  
 medium on the transmitted and incident sides,  $\theta_i$  is the incident  
 light angle,  $\lambda$  is the vacuum wavelength, and  $d\Phi/dx$  is the phase  
 gradient. In our case,  $d\Phi$  equals  $\pi/4$  and  $dx$  equals the unit cell  
 size of 190 nm. Hence we expect that the gradient metasurfaces  
 will deflect the transmitted beam at an angle of  $20.48^\circ$  to  
 normal incidence.

We first performed a finite-difference time-domain (FDTD)  
 simulation of the gradient metasurfaces. We observe that the  
 light excites Fabry–Pérot-type resonances in each post (Figure  
 3a). As shown in Figure 3b, the diffraction angle observed from  
 the phase profile is  $20.48^\circ$ . The same angle can also be  
 calculated from Figure 3c by<sup>37</sup>

$$\theta = \sin^{-1}(k_x/k_0) = \sin^{-1}(0.35) = 20.48^\circ \quad (2)$$

Further, we obtain a transmission efficiency of 61% at 532  
 nm and an efficiency for the diffraction into the desired order of  
 97%. Here, these transmission and diffraction efficiencies are  
 defined as<sup>11,17</sup>

$$\eta_T = I_{\text{out}}/I_{\text{input}} \quad (3)$$

$$\eta_{\text{diff}} = I_{1\text{rd}}/I_{\text{out}} \quad (4)$$

where  $I_{\text{input}}$  is the transmission intensity of the quartz substrate  
 and  $I_{\text{out}}$  and  $I_{1\text{rd}}$  are the total transmission intensity and the +1  
 order diffraction intensity in transmission of the metasurfaces,  
 respectively. We also define the deflection efficiency as

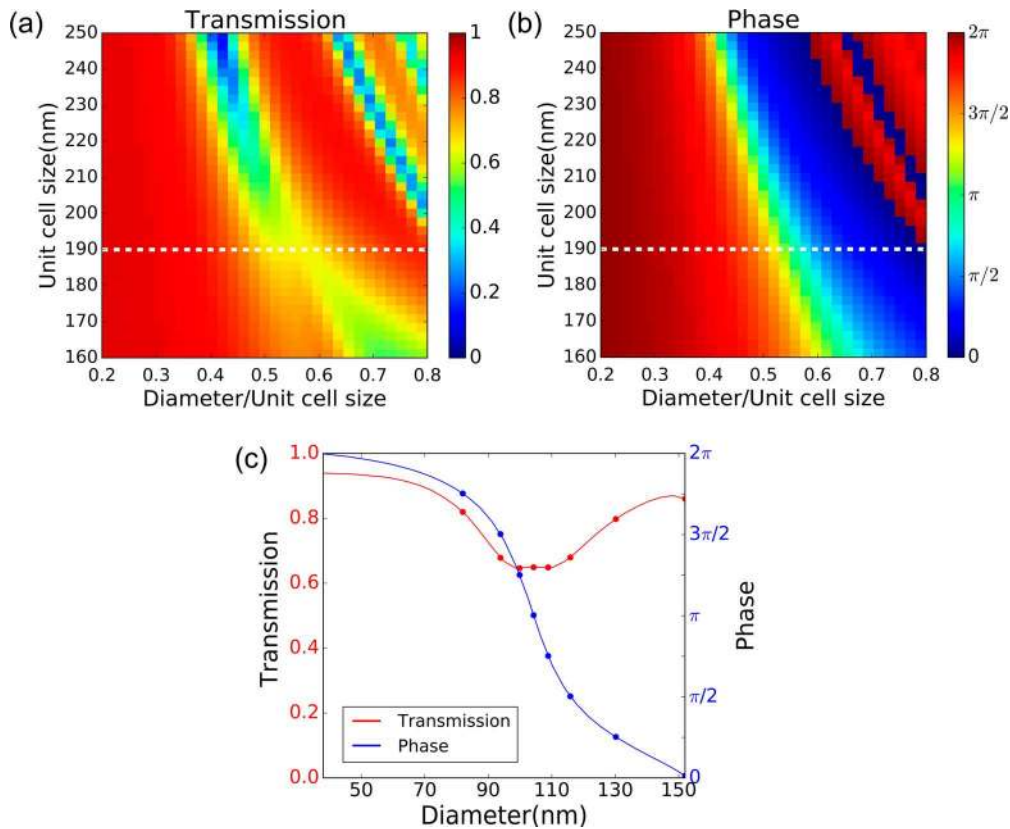


**Figure 2.** Calculation of (a) the transmission and (b) the phase of the periodic c-silicon posts on a square lattice with different unit cell size and diameters. (c) Transmission and phase of the periodic c-silicon posts with 190 nm unit cell size and 220 nm height for different diameters.

**Table 1. Diameters of Posts with 190 nm Unit Cell Size and 220 nm Height Required to Achieve Full  $2\pi$  Coverage in  $\pi/4$  Steps**

	phase (rad)							
	0	$\pi/4$	$\pi/2$	$3\pi/4$	$\pi$	$5\pi/4$	$3\pi/2$	$7\pi/4$
diameter (nm)	152	130	116	109	104	100	94	82

$$\eta = I_{\text{rd}}/I_{\text{input}} \quad (5)$$

being equal to the product of diffraction efficiency and transmission efficiency into the desired diffraction order.

The difference between unity and the observed deflection efficiencies (59%) is mainly caused by the absorption of c-silicon (30%), interface reflectivity (8%), and other diffraction orders (3%). For the 220 nm film used here, the aspect ratio of the fabricated device is 2.7. As shown in Figure 4a, we have calculated the transmission efficiency and diffraction efficiency as a function of c-silicon thickness. For thin c-silicon, it is difficult to achieve full  $2\pi$  phase control for high diffraction efficiency and transmission, while for thicker c-silicon, the aspect ratio is too high, leading to high absorption and fabrication complexity. It is interesting to note that if we were to use a slightly thicker film of 250 nm and a 3.4 aspect ratio, we could increase the transmission further to 73% (Figure 4b,c) even though the silicon is an absorbing material at that wavelength. Furthermore, the value is close to the result of 78% obtained with polarization-independent metasurfaces by  $\text{TiO}_2$ <sup>31</sup> and which requires a much higher aspect ratio and hence more demanding fabrication.

We also simulated the full-width at half-maximum (fwhm) of the diffraction efficiency for both the 220 and 250 nm metasurfaces made in c-silicon and a-silicon in Figure S3 of the Supporting Information. We obtain bandwidths around 100 and 65 nm fwhm for the c-silicon and the a-silicon metasurfaces, respectively.

Thin-film c-silicon from an SOI wafer can be transferred to a rigid or a flexible substrate using a lift-off and stamp printing process<sup>38,39</sup> or by adhesive wafer bonding and deep reactive ion etching (DRIE).<sup>40,41</sup> We used the latter method because we found it easier to maintain the integrity of the nanostructure. We then used electron beam lithography (EBL) to define the pattern. Our fabrication process is illustrated in Figure 5.

First, we deposit 1  $\mu\text{m}$  silica on a SOITEC SOI wafer comprising a 220 or 250 nm thin-film c-silicon layer on 2  $\mu\text{m}$  of silica. This 1  $\mu\text{m}$  silica layer protects the c-silicon from the adhesives and quartz (Figure 5a). Next, we spin the UV curable adhesive NOA61 on the sample followed by bonding to the quartz substrate (Figure 5b and c). Then the sample is illuminated by 365 nm ultraviolet LED light to cross-link the NOA61 polymer for 2 h. In order to obtain optimum adhesion, the sample is baked at 50  $^\circ\text{C}$  for 2 days (Figure 5d). The silicon substrate is then removed by first milling down to near 40  $\mu\text{m}$  followed by DRIE (Figure 5e). Finally, the c-silicon on quartz substrate is obtained by removing the silica of the SOI wafer using HF acid.

The fabrication process of the metasurfaces on the c-silicon by EBL is shown in Figure Sg–i. The sample is spin-coated with 180 nm ZEP520A electron beam resist followed by a 50 nm aluminum layer (thermal evaporation) to serve as the charge dissipation layer. The pattern is then exposed using a 193

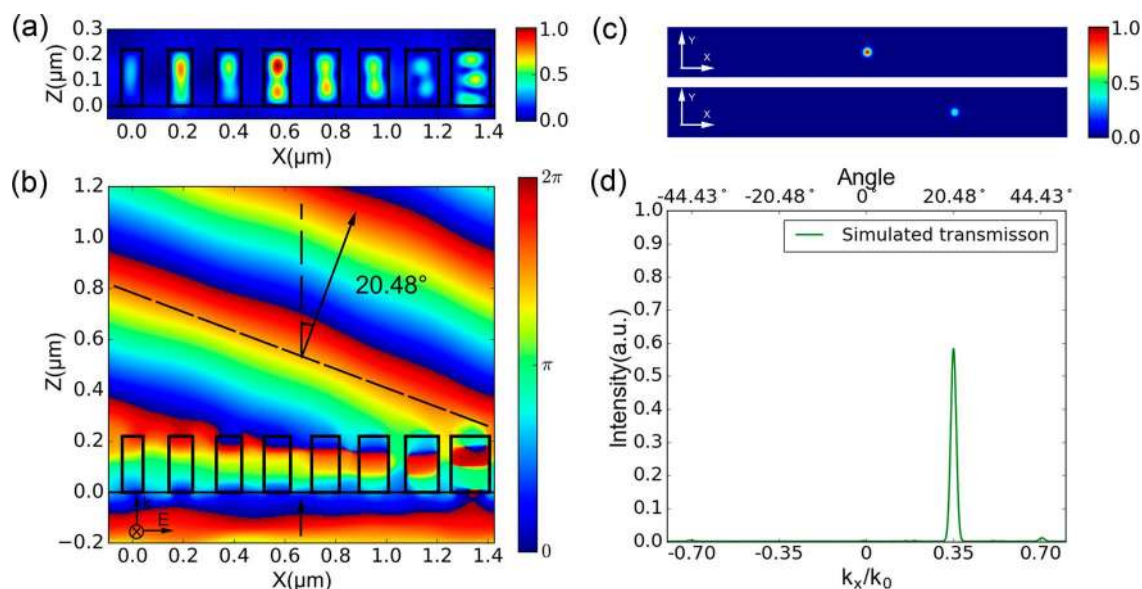


**Figure 3.** FDTD simulation of the gradient metasurface. (a) Mode profile for each 220 nm thick c-silicon post of the deflector, showing the magnetic field amplitude in the  $xz$  plane ( $H_{xz}$ ) for a wavelength of 532 nm. We start with the smallest post on the left and gradually increase the size toward the largest post on the right. (b) Phase profile obtained by the metasurface resulting in a diffraction angle of  $20.48^\circ$ . (c) Far-field profiles of the incident light intensity (top) and transmission intensity (bottom). (d) Transmitted deflected beam intensity normalized to the input signal in the  $k_x$  direction.

194 Raith Viste EBPG-5000plusES electron beam writer at 100  
 195 keV. After exposure, the aluminum layer is removed by  
 196 tetramethylammonium hydroxide and the resist is developed  
 197 with xylene. Then the pattern transfer is etched using an  
 198 Oxford Instruments inductively coupled plasma tool.

199 The overall area of the fabricated gradient metasurface is 200  
 200  $\mu\text{m} \times 200 \mu\text{m}$ . As shown in Figure 6a, we used a 532 nm cw  
 201 laser for illumination, linear polarizers, and a half-wave plate to  
 202 change the polarization direction of the input light. A 4 $\times$   
 203 objective (Obj1, 0.1 NA) was used to focus the light onto the  
 204 sample with a spot diameter of  $\sim 150 \mu\text{m}$ . A 100 $\times$  objective  
 205 (Obj2, 0.9 NA) was used to collect the transmitted signal. The  
 206 real-space and  $k$ -space (diffraction order) image of the sample  
 207 was captured by the CCD, respectively (Figure 6a). From  
 208 Figure 6b and c, we can see that the metasurface directs the  
 209 light almost entirely into the +1 order, while the other  
 210 diffraction orders are too weak to be captured by the CCD. The  
 211 diffraction angle is measured to be  $21^\circ$ , which is close to the  
 212 theoretical calculation and the numerical simulation. For the  
 213 220 nm thin film c-silicon design, the transmission efficiency  
 214 and the diffraction efficiency are measured to be 51% and 93%  
 215 by using the intensity value measured by the optical power  
 216 meter. As predicted by theory, the measured transmission  
 217 efficiency was polarization-independent with only 5% variation  
 218 (Figure 6d). This small variation may come not only from  
 219 fabrication imperfections but also from cross-talk between  
 220 different meta-atoms in the array.<sup>25</sup> For the 250 nm thin film c-  
 221 silicon design, the transmission efficiency and the diffraction  
 222 efficiency can be improved to be 71% and 95% in the  
 223 experiment (Figure 6e).

224 It is known that the transmission efficiency of plasmonic  
 225 metasurfaces is limited to 25%<sup>16</sup> because of ohmic loss, which is  
 226 absent in dielectric metasurfaces. In order to highlight the  
 227 improvement achieved with different types of dielectric  
 228 metasurfaces, we compare the experimental transmission in  
 229 ~~the near-infrared and~~ the visible regime in Table 2. The  
 230 deflection efficiency is defined as above (eq 5), being equal to

the product of diffraction efficiency and transmission efficiency. 231  
 The aspect ratio is defined as the ratio of the minimum feature size 232  
 of the nanostructure to the thickness of the material. 233

As shown in Table 2, low-index-contrast metasurfaces such as 234  
 quartz<sup>35</sup> and  $\text{TiO}_2$ <sup>31</sup> offer higher transmission in the visible 235  
 regime, but they also require higher thickness and very high 236  
 aspect ratios to achieve a full 0 to  $2\pi$  phase range for 237  
 polarization-independent operation. For example, the quartz 238  
 structure requires an aspect ratio of 10 for 633 nm operation, 239  
 which makes it difficult to fabricate precisely. Poly-silicon and 240  
 a-silicon metasurfaces can be fabricated much more easily due to 241  
 their higher refractive index and lower aspect ratios. But the 242  
 deflection efficiency is limited in the shorter wavelength range 243  
 because of absorption loss, and reported efficiencies are below 244  
 30% at 500 nm even for polarization-dependent designs.<sup>17</sup> By 245  
 improving the structure, Yu et al.<sup>11</sup> demonstrated a 45% 246  
 deflection efficiency at 705 nm in a-silicon, but were not able to 247  
 obtain high efficiency at 500 nm, which is very important for 248  
 display applications. By comparison, c-silicon metasurfaces offer 249  
 significant advantages compared to these materials. Metasurfaces 250  
 based on c-Si operate with a thinner film and a lower aspect 251  
 ratio than  $\text{TiO}_2$ , and they achieve better transmission than poly- 252  
 silicon and a-silicon in the visible regime. On the basis of a 253  
 simple transfer technique, the c-silicon can be easily transferred 254  
 to the desired substrate from an SOI wafer. Due to its high 255  
 refractive index, the c-silicon pattern can be easily fabricated 256  
 and surrounded with other low-index materials to increase the 257  
 numerical aperture of metalenses and flexible metasurfaces.<sup>37,42</sup> 258

Having now experimentally demonstrated a deflection 259  
 efficiency of 47%, let us consider further improvements. First 260  
 of all, we note a discrepancy of 12% between the simulated 261  
 efficiency (59%, Figure 3c) and the experimental value. This 262  
 discrepancy can be explained by fabrication tolerances; by 263  
 analyzing the as-fabricated structures, we note an average size 264  
 discrepancy in pillar diameter of 7 nm. If we use this adjusted 265  
 size in our simulation, the calculated efficiency becomes 45%, 266  
 i.e., similar to the experimental value within measurement error. 267

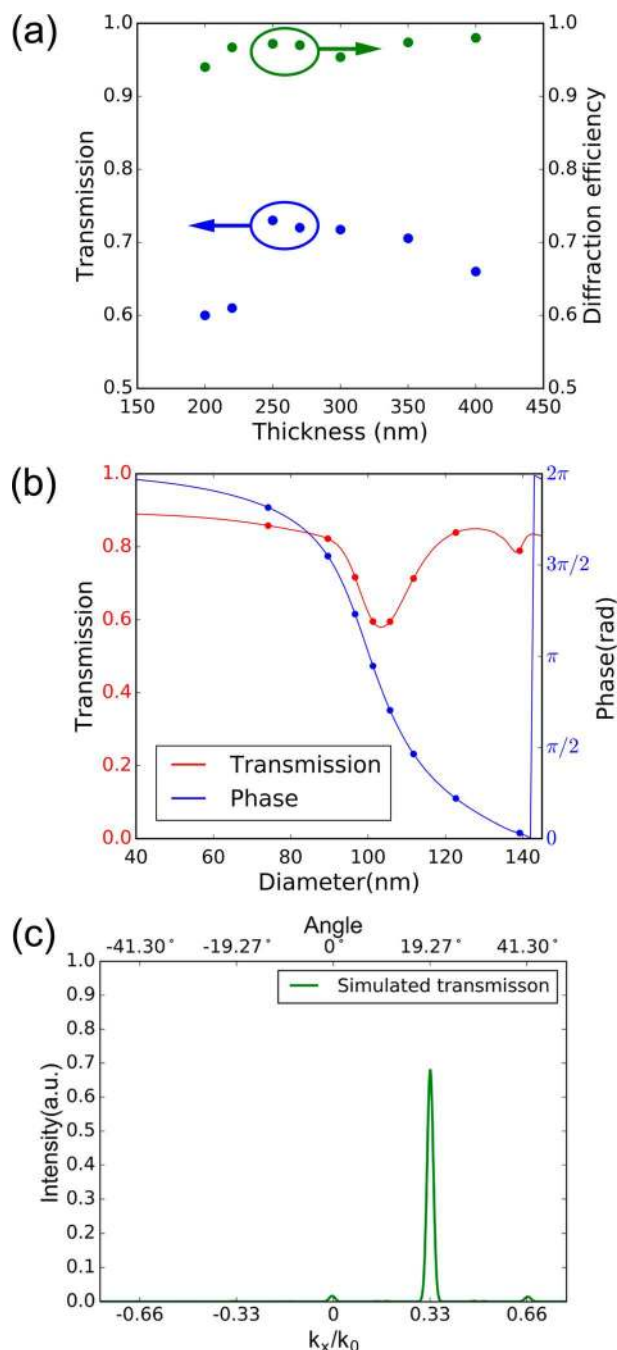


**Figure 4.** Calculation of (a) the transmission efficiency and diffraction efficiency of the deflectors as a function of c-silicon thickness. The corresponding metasurface designs are shown in Table S1. (b) Transmission and phase of the periodic c-silicon posts with 200 nm unit cell size for 250 nm film thickness. (c) FDTD simulation of the transmitted beam intensity normalized to the input signal in the  $k_x$  direction for the 250 nm thick film.

268 It is therefore realistic to achieve the predicted 59% value with a  
 269 reduction in fabrication tolerances. Second, high-aspect-ratio  
 270 nanostructures can achieve large phase delay easily and obtain  
 271 high deflection efficiency. On the other hand, increased  
 272 thickness will also increase the absorption of the posts and  
 273 fabrication complexity. We found that 250 nm thickness c-  
 274 silicon posts happen to be the sweet spot to balance these two  
 275 effects and achieve the highest deflection efficiency at 532 nm.  
 276 Hence, we have demonstrated that an increase in film thickness

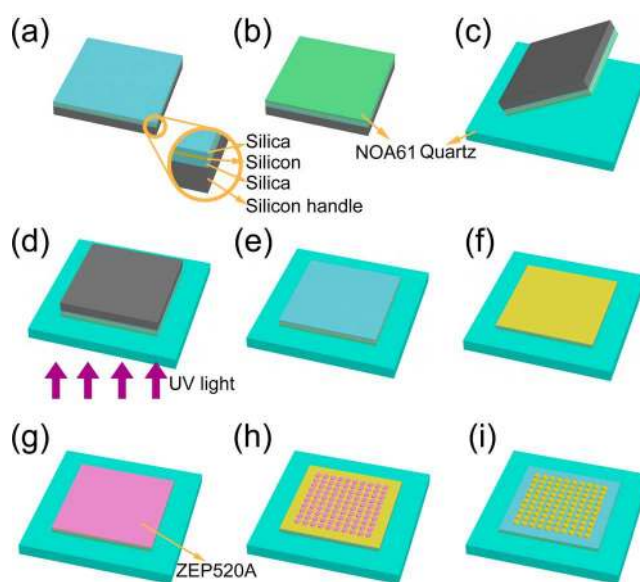


**Figure 5.** Schematic illustration of the c-silicon transfer process and sample fabrication. (a) Deposition of silica on an SOI wafer using ICP-CVD. (b) Spin-coating adhesive NOA61 (c) Bonding SOI with fused quartz. (d) Exposing with UV light for 2 h, followed by baking for 2 days at 50 °C. (e) Polishing the silicon substrate to ~40 μm, then removing the remaining silicon substrate by DRIE. (f) Removing the silica layer with HF acid. (g) Spinning ZEP520A and depositing Al. (h) Exposing the pattern by EBL and removing Al. (i) Transferring the pattern to silicon by ICP, then removing the resist by 1165 remover and O<sub>2</sub> plasma ashing.

to 250 nm allows us to push the efficiency even further, i.e., up  
 277 to 71% in simulation (Figure 4b) and 67% in experiment  
 278 (Figure 6e). Demonstrating the possibility of achieving such a  
 279 high efficiency for visible light with silicon is a truly surprising  
 280 outcome of this work. We verify that diameter variations are  
 281 indeed responsible for the discrepancy between simulation and  
 282 experiment, as the variations are smaller for the 250 nm sample  
 283 and, correspondingly, the discrepancy is smaller as well.  
 284

In summary, we have transferred thin-film c-silicon onto a  
 285 quartz substrate by adhesive wafer bonding, then demonstrated  
 286 c-silicon gradient metasurfaces for beam deflection at a  
 287 wavelength of 532 nm. Furthermore, our experiment  
 288 demonstrates full  $2\pi$  phase control. We demonstrate a  
 289 polarization-independent transmission efficiency of 71% with  
 290 95% diffraction efficiency. The corresponding deflection  
 291 efficiency is 67%, and our simulations show that it can be  
 292 increased up to 71%, which is very close to the values achieved  
 293 with TiO<sub>2</sub>, yet with a lower aspect ratio, hence reduced  
 294 fabrication complexity, if we use commercially available silicon  
 295 on glass samples.<sup>44,45</sup> This lower aspect ratio also achieved high  
 296 phase delay while reducing the absorption and fabrication  
 297 complexity, which make it possible to achieve high efficiency  
 298 metasurfaces comparable with TiO<sub>2</sub>.  
 299

We believe that this approach not only can be applied to  
 300 other wavefront shaping situations, such as focusing, vortex  
 301 generation, and holography, but also offers a viable route to  
 302 efficient tunable metasurfaces on flexible substrates in the  
 303 visible range. Our geometry is also attractive for a variety of  
 304 applications in integrated optics, such as imaging, biomedical  
 305 sciences, or wearable consumer electronics.  
 306

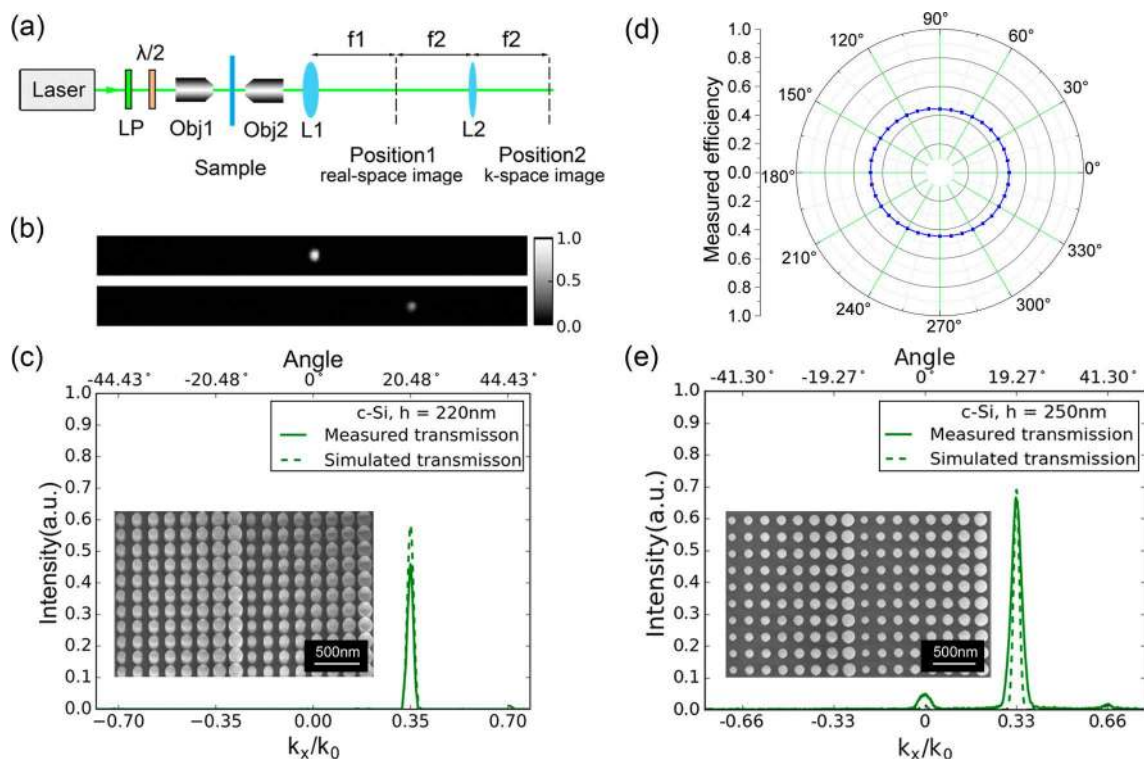


**Figure 6.** (a) Measurement setup used to characterize the metasurfaces according to the design shown in Table 1. (b) Far-field profiles of the incident light intensity (top) and transmitted intensity (bottom) captured by a CCD camera. (c) Experiment (solid line, calculated from the CCD camera data in panel b) and simulation (dashed line, same as Figure 3c) of the transmitted deflected beam intensity normalized to the input signal in the  $k_x$  direction of the 220 nm thin film c-silicon design. The inset shows an SEM micrograph of the structure. (d) Measured transmission efficiency with different polarization directions of the 220 nm thin film c-silicon design. The polarization direction is defined as the angle between the electric field and gradient of the posts. (e) Experiment and simulation of the transmitted deflected beam intensity of the 250 nm thin film c-silicon design.

**Table 2. Summary of Previously Reported Experimental Metasurfaces Used as Deflectors Operating in Transmission in the Visible Range**

ref	material	wavelength	deflection efficiency	polarization	building block	thickness	aspect ratio
Chen et al. <sup>35</sup>	quartz	633 nm	55%	independence	square posts	1.38 $\mu\text{m}$	10
Astilean et al. <sup>43</sup>	TiO <sub>2</sub>	633 nm	85%	linear	1D grating	540 nm	5.3
Lalanne et al. <sup>31</sup>	TiO <sub>2</sub>	633 nm	78%	independence	square posts	487 nm	4.6
Yu et al. <sup>11</sup>	a-silicon	705 nm	45%	independence	circular posts	130 nm	0.93
Lin et al. <sup>17</sup>	p-silicon	500 nm	29%	circular	nanobeams	100 nm	1.2
this work (experiment)	c-silicon	532 nm	47%	independence	circular posts	220 nm	2.47
this work (simulation)	c-silicon	532 nm	59%	independence	circular posts	220 nm	2.7
this work (experiment)	c-silicon	532 nm	67%	independence	circular posts	250 nm	3.4
this work (simulation)	c-silicon	532 nm	71%	independence	circular posts	250 nm	3.4

## 307 ■ ASSOCIATED CONTENT

### 308 ● Supporting Information

309 The Supporting Information is available free of charge on the  
310 ACS Publications website at DOI: 10.1021/acsphtonic-  
311 nics.6b00740.

312 Simulation of the deflecting achieved by our metasurfaces  
313 for c-silicon and a-silicon; the parameter and bandwidth  
314 of our designed metasurfaces. (PDF)

## 315 ■ AUTHOR INFORMATION

### 316 Corresponding Author

317 \*E-mail: wangxueh@mail.sysu.edu.cn.

### 318 ORCID

319 Zhenpeng Zhou: 0000-0001-9712-0866

## Author Contributions

<sup>||</sup>Z. Zhou and J. Li contributed equally to this work.

## Notes

The authors declare no competing financial interest.

## ■ ACKNOWLEDGMENTS

This work is supported by Ministry of Science and Technology  
of China (2016YFA0301300), National Natural Science  
Foundation of China (11674402, 11334015, 11304102),  
Guangzhou Science and Technology Projects  
(201607010044, 201607020023), Natural Science Foundation  
of Guangdong (2016A030312012), the Fundamental Research  
Funds for the Central Universities, the Open Research Project  
of the State Key Laboratory of Optoelectronic Materials and  
Technologies in Sun Yat-Sen University of China, and EPSRC  
of U.K. under Grant EP/J01771X/1 (Structured Light). We

335 also would like to acknowledge Prof. Jianwen Dong for useful  
336 discussions on the metasurface design.

## 337 ■ REFERENCES

- 338 (1) Zheludev, N. I.; Kivshar, Y. S. From metamaterials to  
339 metadevices. *Nat. Mater.* **2012**, *11*, 917–924.
- 340 (2) Meinzer, N.; Barnes, W. L.; Hooper, I. R. Plasmonic meta-atoms  
341 and metasurfaces. *Nat. Photonics* **2014**, *8*, 889–898.
- 342 (3) Yu, N.; Capasso, F. Flat optics with designer metasurfaces. *Nat.*  
343 *Mater.* **2014**, *13*, 139–150.
- 344 (4) Minovich, A. E.; Miroshnichenko, A. E.; Bykov, A. Y.; Murzina, T.  
345 V.; Neshev, D. N.; Kivshar, Y. S. Functional and nonlinear optical  
346 metasurfaces. *Laser Photonics Rev.* **2015**, *9*, 195–213.
- 347 (5) Glybovski, S. B.; Tretyakov, S. A.; Belov, P. A.; Kivshar, Y. S.;  
348 Simovski, C. R. Metasurfaces: From microwaves to visible. *Phys. Rep.*  
349 **2016**, *634*, 1–72.
- 350 (6) Wan, C.; Ho, Y.; Nunez-Sanchez, S.; Chen, L.; Lopez-Garcia, M.;  
351 Pugh, J.; Zhu, B.; Selvaraj, P.; Mallick, T.; Senthilarasu, S.; Cryan, M. J.  
352 A selective metasurface absorber with an amorphous carbon interlayer  
353 for solar thermal applications. *Nano Energy* **2016**, *26*, 392–397.
- 354 (7) West, P. R.; Ishii, S.; Naik, G. V.; Emani, N. K.; Shalae, V. M.;  
355 Boltasseva, A. Searching for better plasmonic materials. *Laser Photonics*  
356 *Rev.* **2010**, *4*, 795–808.
- 357 (8) Yu, N.; Genevet, P.; Kats, M. A.; Aieta, F.; Tetienne, J. P.;  
358 Capasso, F.; Gaburro, Z. Light propagation with phase discontinuities:  
359 generalized laws of reflection and refraction. *Science* **2011**, *334*, 333–  
360 337.
- 361 (9) Fattal, D.; Li, J.; Peng, Z.; Fiorentino, M.; Beausoleil, R. G. Flat  
362 dielectric grating reflectors with focusing abilities. *Nat. Photonics* **2010**,  
363 *4*, 466–470.
- 364 (10) Jahani, S.; Jacob, Z. All-dielectric metamaterials. *Nat. Nano-*  
365 *technol.* **2016**, *11*, 23–36.
- 366 (11) Yu, Y. F.; Zhu, A. Y.; Paniagua-Domínguez, R.; Fu, Y. H.;  
367 Luk'yanchuk, B.; Kuznetsov, A. I. High-transmission dielectric  
368 metasurface with  $2\pi$  phase control at visible wavelengths. *Laser*  
369 *Photonics Rev.* **2015**, *9*, 412–418.
- 370 (12) Moitra, P.; Slovick, B. A.; Gang, Y. Z.; Krishnamurthy, S.;  
371 Valentine, J. Experimental demonstration of a broadband all-dielectric  
372 metamaterial perfect reflector. *Appl. Phys. Lett.* **2014**, *104*, 171102.
- 373 (13) Esfandyarpour, M.; Garnett, E. C.; Cui, Y.; McGehee, M. D.;  
374 Brongersma, M. L. Metamaterial mirrors in optoelectronic devices.  
375 *Nat. Nanotechnol.* **2014**, *9*, 542–547.
- 376 (14) Staude, I.; Miroshnichenko, A. E.; Decker, M.; Fofang, N. T.;  
377 Liu, S.; Gonzales, E.; Dominguez, J.; Luk, T. S.; Neshev, D. N.; Brener,  
378 I.; Kivshar, Y. Tailoring directional scattering through magnetic and  
379 electric resonances in subwavelength silicon nanodisks. *ACS Nano*  
380 **2013**, *7*, 7824–7832.
- 381 (15) Decker, M.; Staude, I.; Falkner, M.; Dominguez, J.; Neshev, D.  
382 N.; Brener, I.; Pertsch, T.; Kivshar, Y. S. High-Efficiency Dielectric  
383 Huygens' Surfaces. *Adv. Opt. Mater.* **2015**, *3*, 813–820.
- 384 (16) Arbabi, A.; Horie, Y.; Ball, A. J.; Bagheri, M.; Faraon, A.  
385 Subwavelength-thick lenses with high numerical apertures and large  
386 efficiency based on high-contrast transmitarrays. *Nat. Commun.* **2015**,  
387 *6*, 7069.
- 388 (17) Lin, D.; Fan, P.; Hasman, E.; Brongersma, M. L. Dielectric  
389 gradient metasurface optical elements. *Science* **2014**, *345*, 298–302.
- 390 (18) Klemm, A. B.; Stellinga, D.; Martins, E. R.; Lewis, L.; Huyet, G.;  
391 O'Faolain, L.; Krauss, T. F. Experimental high numerical aperture  
392 focusing with high contrast gratings. *Opt. Lett.* **2013**, *38*, 3410–3413.
- 393 (19) Aieta, F.; Kats, M. A.; Genevet, P.; Capasso, F. Applied optics.  
394 Multiwavelength achromatic metasurfaces by dispersive phase  
395 compensation. *Science* **2015**, *347*, 1342–1345.
- 396 (20) Chong, K. E.; Staude, I.; James, A.; Dominguez, J.; Liu, S.;  
397 Campione, S.; Subramania, G. S.; Luk, T. S.; Decker, M.; Neshev, D.  
398 N.; Brener, I.; Kivshar, Y. S. Polarization-Independent Silicon  
399 Metadevices for Efficient Optical Wavefront Control. *Nano Lett.*  
400 **2015**, *15*, 5369–5374.
- 401 (21) Shalae, M. I.; Sun, J.; Tsukernik, A.; Pandey, A.; Nikolskiy, K.;  
402 Litchinitser, N. M. High-Efficiency All-Dielectric Metasurfaces for

- Ultracompact Beam Manipulation in Transmission Mode. *Nano Lett.* **2015**, *15*, 6261–6266. 403
- (22) Khorasaninejad, M.; Ambrosio, A.; Kanhaiya, P.; Capasso, F. 404  
Broadband and chiral binary dielectric meta-holograms. *Sci. Adv.* **2016**, 405  
*2*, e1501258. 406
- (23) Wang, B.; Dong, F.; Li, Q. T.; Yang, D.; Sun, C.; Chen, J.; Song, 407  
Z.; Xu, L.; Chu, W.; Xiao, Y. F.; Gong, Q.; Li, Y. Visible-Frequency 408  
Dielectric Metasurfaces for Multiwavelength Achromatic and Highly 409  
Dispersive Holograms. *Nano Lett.* **2016**, *16*, 5235–5240. 410
- (24) Chong, K. E.; Wang, L.; Staude, I.; James, A. R.; Dominguez, J.; 411  
Liu, S.; Subramania, G. S.; Decker, M.; Neshev, D. N.; Brener, I.; 412  
Kivshar, Y. S. Efficient Polarization-Insensitive Complex Wavefront 413  
Control Using Huygens' Metasurfaces Based on Dielectric Resonant 414  
Meta-atoms. *ACS Photonics* **2016**, *3*, 514–519. 415
- (25) Li, Q.-T.; Dong, F.; Wang, B.; Gan, F.; Chen, J.; Song, Z.; Xu, 416  
L.; Chu, W.; Xiao, Y.-F.; Gong, Q.; Li, Y. Polarization-independent and 417  
high-efficiency dielectric metasurfaces for visible light. *Opt. Express* 418  
**2016**, *24*, 16309. 419
- (26) Yang, Y.; Wang, W.; Boulesbaa, A.; Kravchenko, I.; Briggs, D. 420  
P.; Poretzky, A.; Geohegan, D.; Valentine, J. Nonlinear Fano-Resonant 421  
Dielectric Metasurfaces. *Nano Lett.* **2015**, *15*, 7388–7393. 422
- (27) Arbabi, A.; Horie, Y.; Bagheri, M.; Faraon, A. Dielectric 423  
metasurfaces for complete control of phase and polarization with 424  
subwavelength spatial resolution and high transmission. *Nat. Nano-* 425  
*technol.* **2015**, *10*, 937–943. 426
- (28) Backlund, M. P.; Arbabi, A.; Petrov, P. N.; Arbabi, E.; Saurabh, 427  
S.; Faraon, A.; Moerner, W. E. Removing Orientation-Induced 428  
Localization Biases in Single-Molecule Microscopy Using a Broadband 429  
Metasurface Mask. *Nat. Photonics* **2016**, *10*, 459–462. 430
- (29) Palik, E. D. *Handbook of Optical Constants of Solids*; Academic 431  
Press: San Diego, 1985. 432
- (30) Evlyukhin, A. B.; Novikov, S. M.; Zywietz, U.; Eriksen, R. L.; 433  
Reinhardt, C.; Bozhevolnyi, S. I.; Chichkov, B. N. Demonstration of 434  
magnetic dipole resonances of dielectric nanospheres in the visible 435  
region. *Nano Lett.* **2012**, *12*, 3749–3755. 436
- (31) Lalanne, P.; Astilean, S.; Chavel, P.; Cambil, E.; Launois, H. 437  
Blazed binary subwavelength gratings with efficiencies larger than 438  
those of conventional échelette gratings. *Opt. Lett.* **1998**, *23*, 1081. 439
- (32) Khorasaninejad, M.; Chen, W. T.; Devlin, R. C.; Oh, J.; Zhu, A. 440  
Y.; Capasso, F. Metalenses at visible wavelengths: Diffraction-limited 441  
focusing and subwavelength resolution imaging. *Science* **2016**, *352*, 442  
1190–1194. 443
- (33) Khorasaninejad, M.; Zhu, A. Y.; Roques-Carmes, C.; Chen, W. 444  
T.; Oh, J.; Mishra, I.; Devlin, R. C.; Capasso, F. Polarization- 445  
Insensitive Metalenses at Visible Wavelengths. *Nano Lett.* **2016**, *16*, 446  
7229–7234. 447
- (34) Zhan, A.; Colburn, S.; Trivedi, R.; Fryett, T. K.; Dodson, C. M.; 448  
Majumdar, A. Low-Contrast Dielectric Metasurface Optics. *ACS* 449  
*Photonics* **2016**, *3*, 209–214. 450
- (35) Chen, F. T.; Craighead, H. G. Diffractive phase elements based 451  
on two-dimensional artificial dielectrics. *Opt. Lett.* **1995**, *20*, 121–123. 452
- (36) Li, L. New formulation of the Fourier modal method for crossed 453  
surface-relief gratings. *J. Opt. Soc. Am. A* **1997**, *14*, 2758. 454
- (37) Ee, H. S.; Agarwal, R. Tunable Metasurface and Flat Optical 455  
Zoom Lens on a Stretchable Substrate. *Nano Lett.* **2016**, *16*, 2818– 456  
2823. 457
- (38) Meitl, M. A.; Zhu, Z.-T.; Kumar, V.; Lee, K. J.; Feng, X.; Huang, 458  
Y. Y.; Adesida, I.; Nuzzo, R. G.; Rogers, J. A. Transfer printing by 459  
kinetic control of adhesion to an elastomeric stamp. *Nat. Mater.* **2006**, 460  
*5*, 33–38. 461
- (39) Xu, X.; Subbaraman, H.; Hosseini, A.; Lin, C. Y.; Kwong, D.; 462  
Chen, R. T. Stamp printing of silicon-nanomembrane-based photonic 463  
devices onto flexible substrates with a suspended configuration. *Opt.* 464  
*Lett.* **2012**, *37*, 1020–1022. 465
- (40) Niklaus, F.; Stemme, G.; Lu, J. Q.; Gutmann, R. J. Adhesive 466  
wafer bonding. *J. Appl. Phys.* **2006**, *99*, 031101. 467
- (41) Zabolocki, M. J.; Sharkawy, A.; Ebil, O.; Prather, D. W. 468  
Nanomembrane transfer process for intricate photonic device 469  
applications. *Opt. Lett.* **2011**, *36*, 58–60. 470



- 472 (42) Zhu, L.; Kapraun, J.; Ferrara, J.; Chang-Hasnain, C. J. Flexible  
473 photonic metastructures for tunable coloration. *Optica* **2015**, *2*, 255.
- 474 (43) Astilean, S.; Lalanne, P.; Chavel, P.; Cambil, E.; Launois, H.  
475 High-efficiency subwavelength diffractive element patterned in a high-  
476 refractive-index material for 633 nm. *Opt. Lett.* **1998**, *23*, 552–554.
- 477 (44) Kim, H. S.; Blick, R. H.; Kim, D. M.; Eom, C. B. Bonding  
478 silicon-on-insulator to glass wafers for integrated bio-electronic  
479 circuits. *Appl. Phys. Lett.* **2004**, *85*, 2370–2372.
- 480 (45) MEMS Engineering and Material Home Page. [http://www.](http://www.memseengineering.com)  
481 [memseengineering.com](http://www.memseengineering.com) (accessed January 30, 2017).